

Electronic Supplementary Material (ESI) for Journal of Materials Chemistry C.

Electronic Supplementary Information

High pyroelectric performance by ferroelectric-antiferroelectric transition near room temperature

Ling Li,^a Hui Liu,^b Rui-Xue Wang,^a Haibo Zhang,^c Houbing Huang,^d Ming-Hui Lu,^a Shan-Tao Zhang,^{*a} Shenglin Jiang,^e Di Wu,^a and Yan-Feng Chen^a

^aNational Laboratory of Solid State Microstructures, Department of Materials Science and Engineering, College of Engineering and Applied Science & Jiangsu Key Laboratory of Artificial Functional Materials & Collaborative Innovation Center of Advanced Microstructures, Nanjing University, Nanjing 210093, China. E-mail: stzhang@nju.edu.cn

^bSchool of Mathematics and Physics, University of Science and Technology Beijing, Beijing 100083, China

^cSchool of Materials Science and Engineering, State Key Laboratory of Material Processing and Die & Mould Technology, Huazhong University of Science and Technology, Wuhan 430074, China

^dAdvanced Research Institute of Multidisciplinary Science, Beijing Institute of Technology, Beijing 100081, China

^eSchool of Optical and Electronic Information, Huazhong University of Science and Technology, Wuhan 430074, China

Experimental Section

Synthesis of $(1-x)\text{Pb}_{0.99}\text{Nb}_{0.02}[(\text{Zr}_{0.57}\text{Sn}_{0.43})_{0.937}\text{Ti}_{0.063}]_{0.98}\text{O}_3-x\text{ZnO}$ (PNZST- $x\text{ZnO}$, $0 \leq x \leq 0.40$), ZnO , and $(1-x)\text{BaTiO}_3-x\text{ZnO}$ ($\text{BaTiO}_3-x\text{ZnO}$, $0 \leq x \leq 0.20$)

PNZST- $x\text{ZnO}$ composites were synthesized by solid state reaction. Firstly, PbO (99.9%), Nb_2O_5 (99.0%), ZrO_2 (99.8%), SnO_2 (99.8%) and TiO_2 (99.0%, all from Alfa Aesar), were weighed according to the stoichiometric formula and ball milled in ethanol for 24 h. The dried slurries were calcined at 850 °C for 4 h with an increasing and decreasing temperature rate of 5 °C min⁻¹, ground by hand for 20 min, ball milled again in ethanol for 24 h, and dried again. The dried powders were sintered in covered alumina crucibles at 1200 °C for 4 h and then ground by hand for 1.0 h. In this way, single phase PNZST powders were obtained.

Afterwards, both the prepared PNZST powder and the commercial ZnO nanoparticle with the size of 25 nm (PlasmaChem, Germany) were weighed according to the formula of PNZST- $x\text{ZnO}$ with $x = 0, 0.025, 0.05, 0.06, 0.07, 0.08, 0.09, 0.1, 0.2, 0.3$ and 0.4 . Each mixture was ball milled in ethanol for 24 h, dried and subsequently pressed into green disks with a diameter of 10 mm under 40 MPa. Sintering was carried out in covered alumina crucibles at 1000-1050 °C for 1 h with a rapid increasing and decreasing temperature rate of 9 °C min⁻¹. The $x = 0$ (PNZST) disks were sintered at 1200 °C for 4 h with an increasing and decreasing temperature rate of 5 °C min⁻¹.

ZnO ceramics is prepared. ZnO nanoparticle with the size of 25 nm (PlasmaChem, Germany) were pressed into green disks with a diameter of 10 mm under 40 MPa. Sintering was carried out in covered alumina crucibles at 950-1000 °C for 2 h with a rapid increasing and decreasing temperature rate of 5 °C min⁻¹.

$\text{BaTiO}_3-x\text{ZnO}$ ($0 \leq x \leq 0.20$) composite ceramics is prepared with the similar process with PNZST- $x\text{ZnO}$. Briefly, BaTiO_3 was sintered at 1350 °C for 3 h with an increasing and decreasing temperature rate of 5 °C min⁻¹, and then ground by hand for 1.0 h. In this way, single phase BaTiO_3 powders were obtained. Afterwards, both the prepared BT powder and the commercial ZnO nanoparticle with the size of 25 nm (PlasmaChem, Germany) were weighed according to the formula of $\text{BT}-x\text{ZnO}$ with $x = 0, 0.1$ and 0.2 . Each mixture was ball milled in ethanol for 24 h, dried and subsequently pressed into green disks with a diameter of 10 mm under 40 MPa. Sintering was carried out in covered alumina crucibles at 1150-1200 °C for 1 h with a rapid increasing and decreasing temperature rate of 9 °C min⁻¹.

X-ray diffraction and scanning electron microscopy measurements

The crystal structure of the composites was characterized by powder x-ray diffraction (XRD) with $\text{Cu K}_{\alpha 1}$ source ($\lambda = 0.15406$ nm). Measurement angle (2θ) ranges from 20° to 80° with step size of 0.02° and scanning speed 2°/min. Room temperature XRD measurements were carried out using Rigaku Ultima III while temperature-dependent XRD measurements were performed using PANalytical, PW 3040-X'Pert Pro. Unit cell parameters and volume were fitted by full-profile Le-Bail fitting. The room temperature high resolution synchrotron x-ray diffraction measurements were performed at 11-BM-B at Advanced Photon Source (APS) at

Argonne National Laboratory with X-ray wavelength of 0.41272 Å. The microstructures and element distribution were analyzed by scanning electron microscopy (SEM, Zeiss Ultra 55).

Differential scanning calorimetry (DSC) measurements

In order to calculate values of figure of merits (FOMs), we need to obtain the volume heat specific (C_v) of each composition. DSC measurements were performed on a Netzsch DSC (STA-449C, Netzsch, Germany) under nitrogen atmosphere in aluminum crucibles with a heating or cooling rate of 15 °C/min. The volume heat specific C_v ($C_v = \rho C_p$) of $x = 0, 0.1$ and 0.2 is calculated to be $2.2 \times \text{J} \cdot \text{cm}^{-3} \cdot \text{K}^{-1}$ ($T = 25$ °C), $1.27 \times \text{J} \cdot \text{cm}^{-3} \cdot \text{K}^{-1}$ ($T = 44.5$ °C) and $2.75 \times \text{J} \cdot \text{cm}^{-3} \cdot \text{K}^{-1}$ ($T = 52.4$ °C), respectively. The specimen density was measured by the Archimedes method.

Pyroelectric property measurements

For macroscopic electric properties measurement, the circular surfaces of the ground disks with the diameter of ~8.5 mm and the thickness of ~0.5 mm were covered by a thin layer of silver paste, then fired at 500 °C for 30 min. Each ceramic was poled at room temperature with 4.5 kV/mm for 30 min before pyroelectric measurement.

The pyroelectric property was measured by using the Pyroelectric Test System (PKSPIV17 T, USA) with a Keithley 6485 Picoammeter. The pyroelectric voltage and current for energy harvesting characterization were acquired by a testing system equipped with Keithley 6517B electrometer by a rate of 2 °C·min⁻¹.

It is worth to note that the $T_{\text{FE-AFE}}$ determined from pyroelectric measurements is relatively higher than that from dielectric measurement due to their different heating method. During pyroelectric measurement, the poled sample is placed in a furnace and the sample is heated by thermal radiation, therefore, the actual sample temperature is lower than the recorded temperature. However, during dielectric measurement, the sample is placed on the heater directly, thus the recorded temperature is the actual sample temperature. Accordingly, the temperature in pyroelectric measurement is calibrated based on that determined by dielectric measurement.

Pyroelectric measurements on ZnO and (1-x)BaTiO₃-xZnO ($0 \leq x \leq 0.20$) were carried out with the similar process. Before measurements, the ZnO ceramics were poled with 2 kV/mm for 30 min and the (1-x)BaTiO₃-xZnO ($0 \leq x \leq 0.20$) ceramics were poled with 3 kV/mm for 30 min.

Dielectric and ferroelectric properties measurements

The temperature dependent dielectric constant (ϵ_r) and dielectric loss ($\tan\delta$) were measured using an impedance analyzer (HP4294A) at several frequencies on poled samples (4.5 kV/mm, 30min for PNZST-ZnO and 3 kV/mm for 30 min for BaTiO₃-ZnO, at room temperature). The polarization-electric field (P - E) loops, current-electric field (J - E) curves and strain-electric field (S - E) curves were measured at 1 Hz using a TF analyzer 1000 (AixACCT, Germany) in silicone oil with controllable temperature from 20 °C to 120 °C. The

low temperature ($< 20\text{ }^{\circ}\text{C}$) P - E loops and J - E curves were measured at 1 Hz using another ferroelectric tester (Radiant Premier II, USA).

Piezoelectric property measurements

The room temperature piezoelectric coefficient (d_{33}) was measured on poled ceramics (4.5 kV/mm, 30min at room temperature) by a Berlincourt- d_{33} -meter (ZJ-6A).

Piezoresponse force microscopy (PFM) measurements

The room temperature PFM measurements were carried out by a commercial piezoresponse force microscopy (Asylum Research, Cypher VRS) with high-voltage package. Firstly, the samples were polished to optical standard. Because the domain structure is sensitive to stresses, the polished samples were then annealed without external electric field at $350\text{ }^{\circ}\text{C}$ for 1 h to release the surface stresses involved during the cutting and polish processes. The ferroelectric domain pattern and switching process were revealed by PFM with conductive probes (Nanoworld, EFM).

In-situ high-energy synchrotron x-ray diffraction (SXRD) measurements.

The samples were cut into ceramic bars with dimension of about $5\text{ mm}\times 1\text{ mm}\times 0.6\text{ mm}$ for *in-situ* high-energy SXRD studies which were performed at 11-ID-C at Advanced Photon Source (APS) at Argonne National Laboratory. For SXRD measurement, the wavelength of high-energy x-rays was 0.1173 \AA , and a beam size of $500\times 500\text{ }\mu\text{m}$ was used. The diffraction patterns were measured in forward scattering geometry on a Perkin Elmer amorphous silicon area detector which was placed approximately 2000 mm away from the sample. The direction of electric field was perpendicular to the beam line. The schematic of the experimental setup can be seen in Ref.1. A triangular cycle electric field ($-5\text{ kV/mm} \sim +5\text{ kV/mm}$) with a step of about 0.5 kV/mm was applied on the bulk samples. The Debye rings under different electric field were divided into equidistant sectors at 10° intervals to integrate the diffraction intensities. The integration of one-dimensional diffraction intensity vs. 2θ patterns data was performed by the Fit2d software.

Theoretical Model

The ferroelectric-antiferroelectric phase transitions of ZnO-doped PNZST were investigated based on the Ginzburg-Landau-Devonshire theory. AFE and FE phases are divided into two sublattices, a and b , associated with polarization \vec{P}_a and \vec{P}_b , respectively. If \vec{P}_a and \vec{P}_b are parallel, the material exhibits FE phase, otherwise, if \vec{P}_a and \vec{P}_b are antiparallel, it is AFE phase. When \vec{P}_a and \vec{P}_b are both zero, it is PE phase. The FE and AFE order parameters \vec{p} and \vec{q} are defined as follows,

$$\vec{p} = \frac{1}{2}(\vec{P}_a + \vec{P}_b), \quad \vec{q} = \frac{1}{2}(\vec{P}_a' - \vec{P}_b') \quad (1)$$

In Eq. (1), \vec{P}_a' and \vec{P}_b' are adopted instead of \vec{P}_a and \vec{P}_b to represent AFE order parameter, because, the polarization associated with sublattices of AFE phase are sometimes different from that of FE phase.

The total free energy density of ZnO-doped PNZST system under stress-free boundary conditions can be expressed as.²

$$f_{total}|_{\sigma_{ij}=0} = a_{ij}p_i p_j + a_{ijkl}p_i p_j p_k p_l + a_{ijklmn}p_i p_j p_k p_l p_m p_n + b_{ij}q_i q_j + b_{ijkl}q_i q_j q_k q_l + b_{ijklmn}q_i q_j q_k q_l q_m q_n + t_{ijkl}p_i p_j q_k q_l \quad (2)$$

where p_i and q_i are the i th components of FE and AFE order parameters; a_{ij} , a_{ijkl} , a_{ijklmn} and b_{ij} , b_{ijkl} , b_{ijklmn} are FE and AFE dielectric stiffnesses, respectively. t_{ijkl} are coupling coefficients between the FE and AFE order parameters. σ is i th component of applied stress in Voigt notation; Among all the coefficients, only a_{11} and b_{11} are assumed to be dependent on temperature. According to Curie-Weiss law, $a_{11} = a_0(T - T_{cp})$, and $b_{11} = b_0(T - T_{cq})$, where the transition temperatures of T_{FE-AFE} and T_{AFE-PE} can be defined by $T_{cp} = 273 + 371.9x - 659.2x^2$, and $T_{cq} = 411 + 191.2x - 321x^2$; and a_0 and b_0 are constants; x denotes the ZnO composition. To simplify the model, we only consider one-dimensional calculation, and the Landau free energy expansion coefficients of the FE and AFE phases are obtained by fitting the free energy to the corresponding experimental results and phase diagram data, where $a_0 = 1.27 \times 10^5 J/m^3$, $a_{1111} = -5.868 \times 10^7 J/m^3$, $a_{111111} = 1.1 \times 10^9 J/m^3$, $b_0 = 1.03 \times 10^6 J/m^3$, $b_{1111} = 1.24 \times 10^8 J/m^3$, $b_{111111} = 7.8 \times 10^{16} J/m^3$, $t_{1111} = 1.0 \times 10^{25} J/m^3$.

The total free energy density including the elasticity contribution can be written as,

$$f_{total} = f_{total}|_{\sigma_{ij}=0} + \frac{1}{2}S_{ijkl}\sigma_{ij}\sigma_{kl} - Q_{ijkl}p_i p_j \sigma_{kl} - \Lambda_{ijkl}q_i q_j \sigma_{kl} \quad (3)$$

where S_{ijkl} are the elastic compliance constants; Q_{ijkl} and Λ_{ijkl} are corresponding electrostrictive coefficients; The electrostrictive coefficients are obtained from the experimentally measured lattice parameters by assuming that the lattice parameters are linearly dependent on tensile stress ($Q_{11} = 0.011$, $\Lambda_{11} = 0.0076$). Considering one-dimensional model, transition temperatures of T_{FE-AFE} and T_{AFE-PE} can be rewritten as: $T_{FE-AFE} = Q_{11}\sigma/a_0$, $T_{AFE-PE} = \Lambda_{11}\sigma/b_0$, the transition temperatures is linearly dependent on tensile stress.

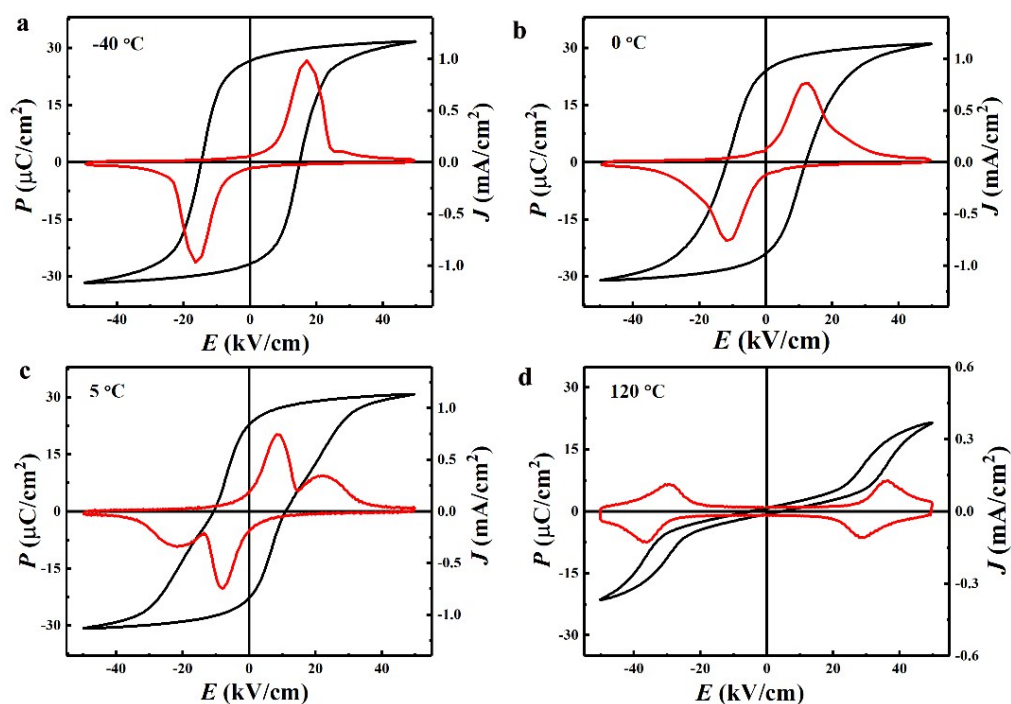


Figure S1. Temperature-dependent P - E loops and J - E loops of $x = 0$ (PNZST) samples measured at different temperature. Below $0\text{ }^{\circ}\text{C}$, the PNZST shows saturated square P - E loop and two-peak J - E curve, which are the typical features of a ferroelectric material.^{3,4} As the temperature increases to $5\text{ }^{\circ}\text{C}$, the P - E loop begins to be pinched with suppressed remnant polarization, and J - E curve show two additional broad current peaks originating from field-induced antiferroelectric-ferroelectric transition,^{4,5} indicating the increased antiferroelectric content. With further increasing temperature, antiferroelectric content tends to be predominant up to $120\text{ }^{\circ}\text{C}$.

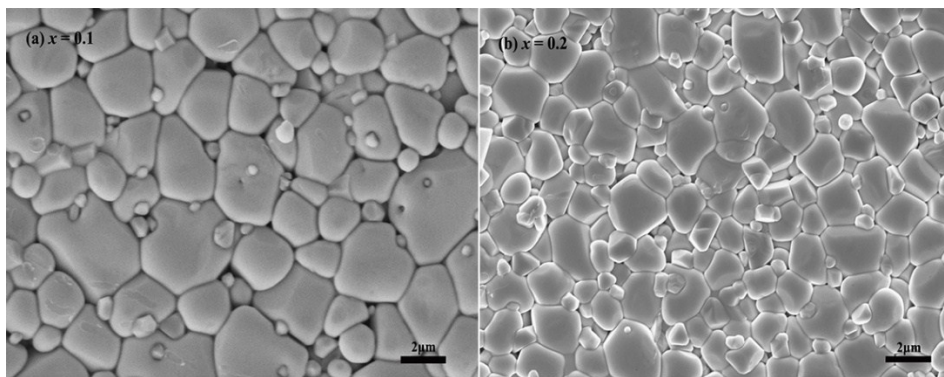


Figure S2 The SEM micrograph of $x = 0.1$ (a) and $x = 0.2$ (b)

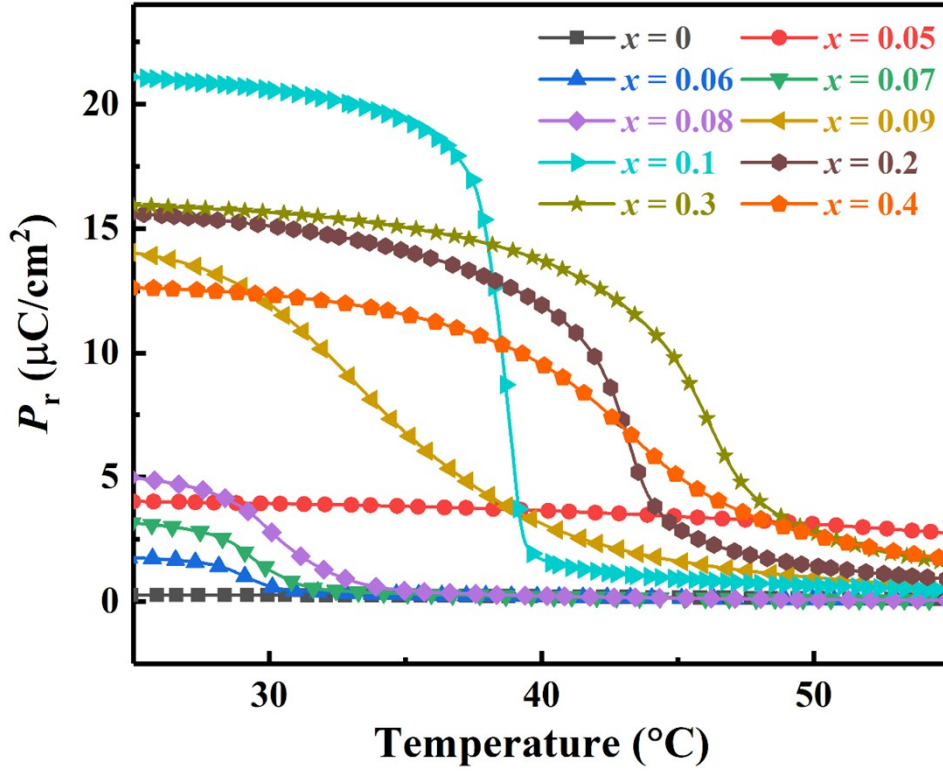


Figure S3. The temperature-dependent calculated remanent polarization P_r by integrating the $J(T)$ for $(1-x)\text{PNZST}-x\text{ZnO}$ ($0 \leq x \leq 0.4$). The pyroelectric coefficient p is defined as the derivative of spontaneous polarization P_r with respect to temperature T ($p = dP_r/dT$). The largest dP_r/dT corresponds to the largest p . It should be noted that for all compositions, the integrated P_r is consistent with that obtained by measuring P - E hysteresis loops.

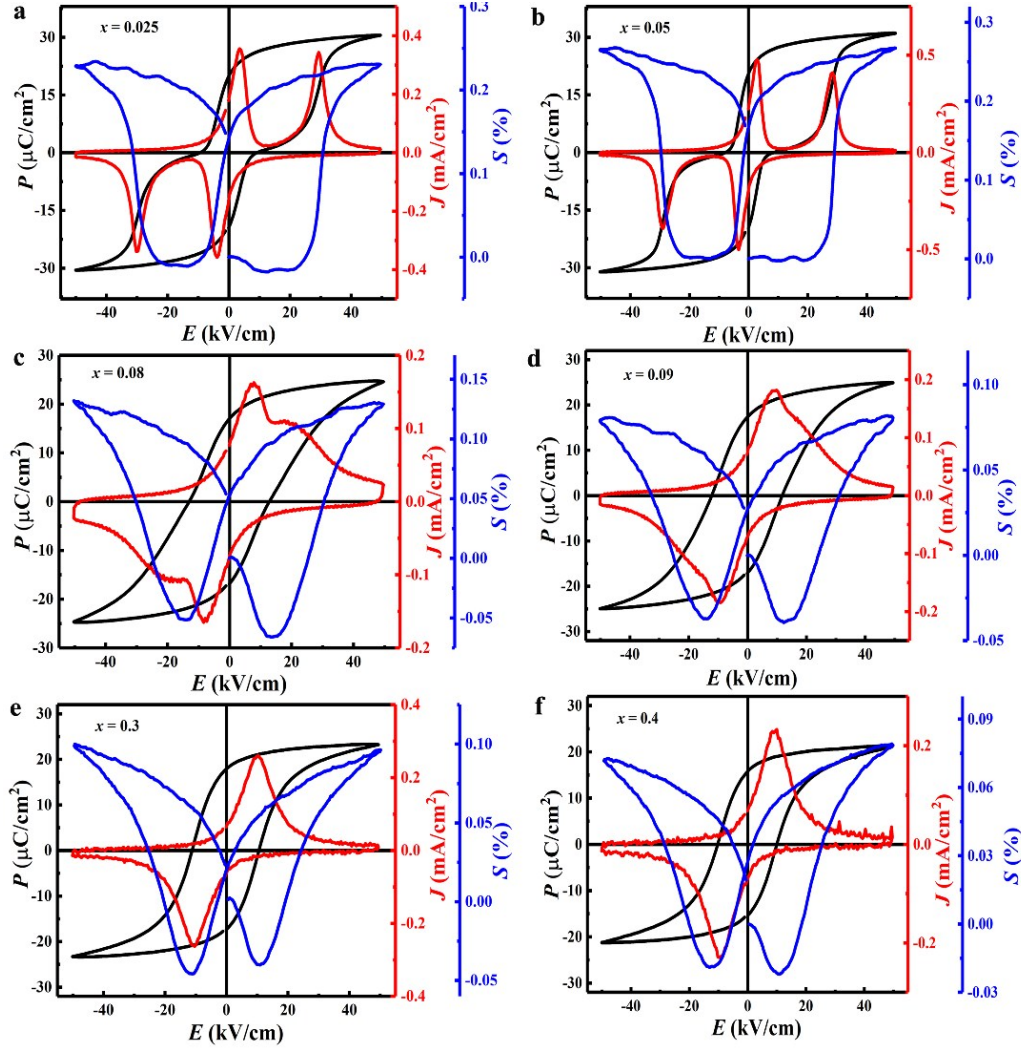


Figure S4. Composition-dependent room temperature P - E loops and J - E loops of $(1-x)$ PNZST- x ZnO ceramics. The compositions with $x \leq 0.05$ show predominant antiferroelectric features of pinched P - E loop, four-peak J - E curve, and almost zero negative strain in S - E curve.^{4,6} When $x \geq 0.08$, ferroelectric phase tends to be predominant due to ferroelectric features of square shaped P - E loop, two-peak J - E curve and larger negative strain in S - E curve.^{3,4,7,8} The saturated polarization P_s and remnant polarization P_r decrease with increasing ZnO content due to reduced content of PNZST.

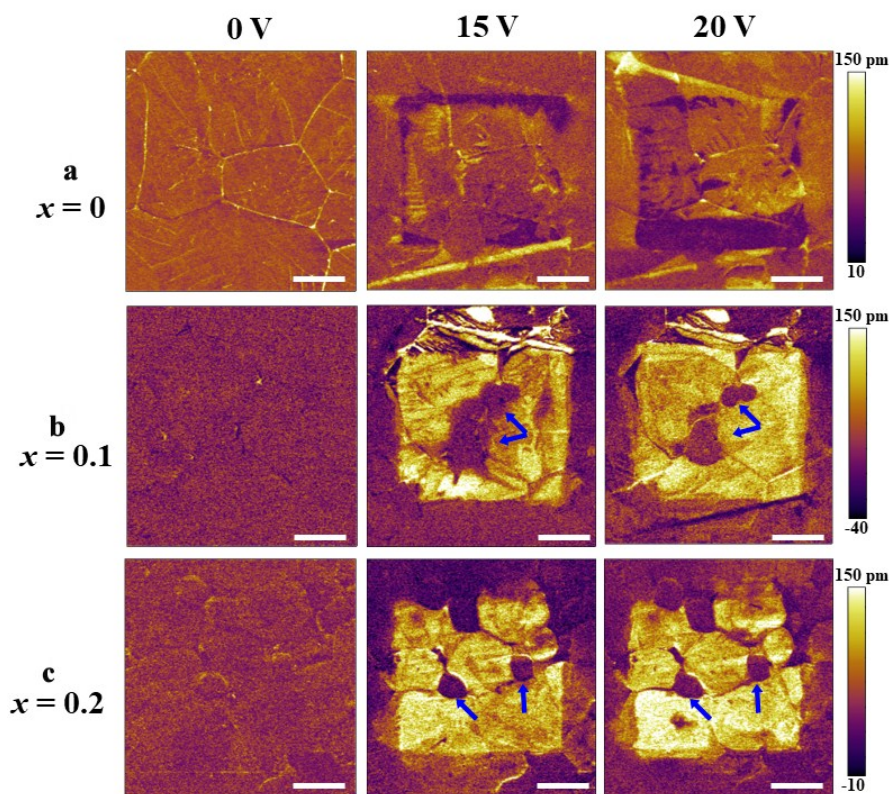


Figure S5. Room temperature out-of-plane PFM amplitude images of $(1-x)\text{PNZST}-x\text{ZnO}$ ($x = 0, 0.1$ and 0.2) ceramics after poling with the DC voltage of 0, 15 and 20 V, respectively. The scanned area is $5 \times 5 \mu\text{m}^2$ and scale bar is $1 \mu\text{m}$. (a) For $x = 0$, weak ferroelectric domain trace can be induced at a large voltage of 20 V, as indicated by the contrast between the interior and external squares, which is consistent with its predominant antiferroelectric nature. However, for (b) $x = 0.1$ and (c) $x = 0.2$, a single domain state is achieved at 15 V, indicating their predominant ferroelectric nature. Besides, as marked with blue arrows, there are small areas without piezoresponse, which are attributed to ZnO particles.

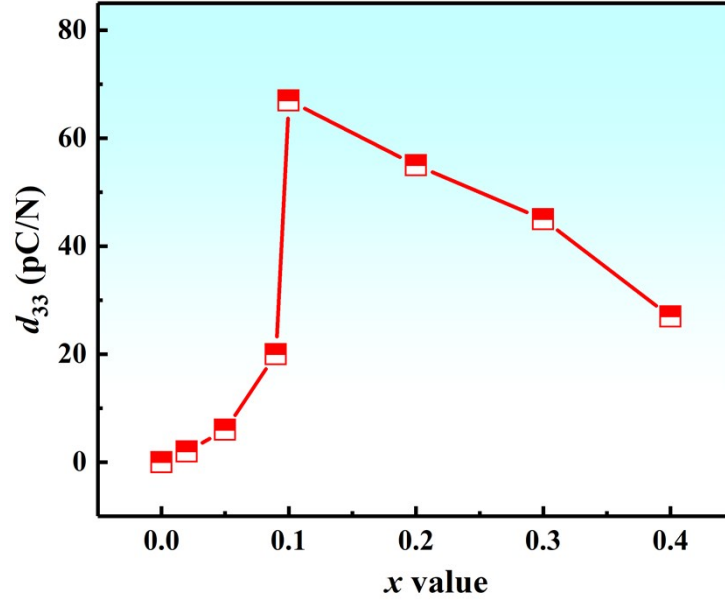


Figure S6. The composition dependent piezoelectric coefficient d_{33} of (1-x)PNZST-xZnO. The $x = 0$ sample shows no piezoelectric effect due to its predominant antiferroelectric nature. The appearance and improvement of piezoelectric effect in PNZST-ZnO composite are mainly due to that the ZnO-induced ferroelectric state. As the result, the d_{33} firstly increases with the increasing content of ZnO, and achieves the largest d_{33} of 67 pC/N at $x = 0.1$. Further decreased d_{33} is attributed to decreased PNZST content.

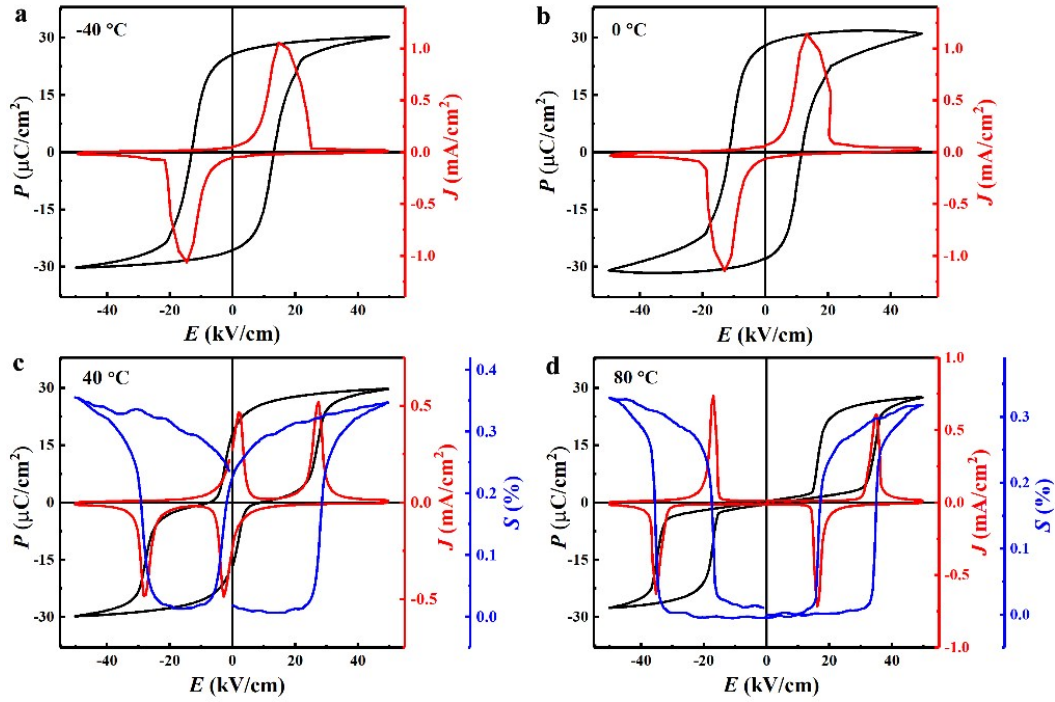


Figure S7. Temperature-dependent P - E , J - E and S - E curves of 0.9PNZST-0.1ZnO composite ceramic. According to other reports^{3-5,6-8} and by considering the room temperature P - E , J - E and S - E shown in Fig. 2, this composite shows typical ferroelectric characteristics for $T \leq 20^\circ\text{C}$. When the temperature reaches 40°C , this composite shows predominant antiferroelectric characteristics. When temperature is further increased up to 80°C , obvious antiferroelectric characteristics are observed. So, it can be concluded that this composite tends to transform from ferroelectric to antiferroelectric order between 20°C - 40°C .

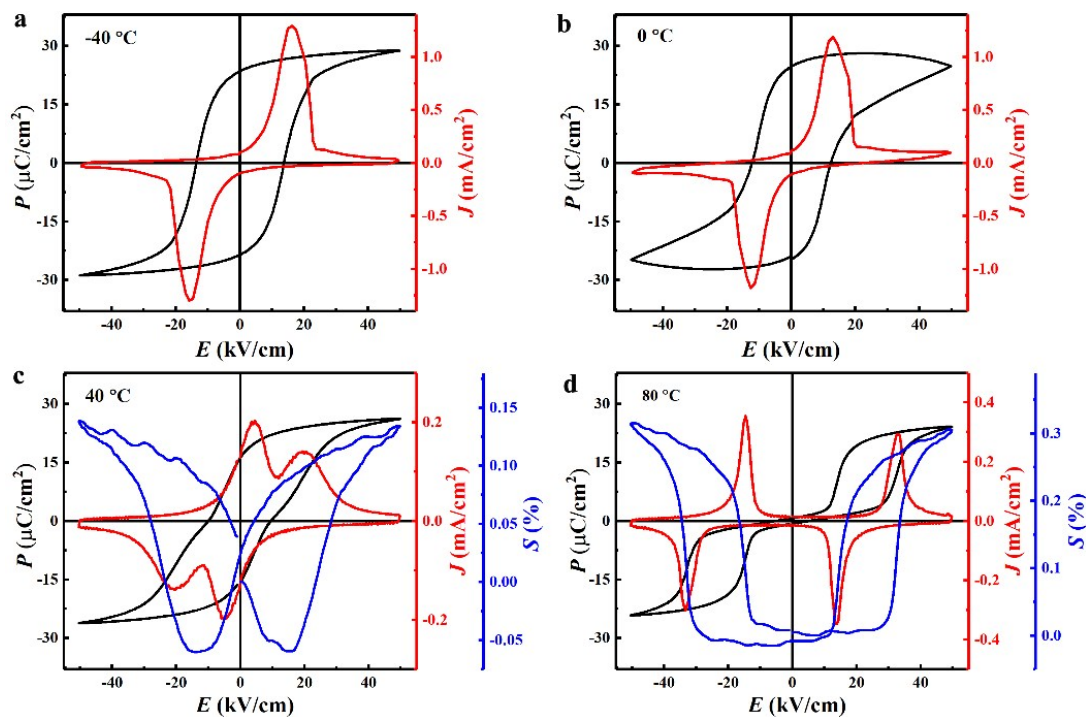


Figure S8. Temperature-dependent P - E , J - E and S - E curves of 0.8PNZST-0.2ZnO composite ceramic. Similar with PNZST-0.1ZnO composite, this composite shows ferroelectric characteristics for $T \leq 20^\circ\text{C}$, and antiferroelectric characteristics tend to appear around 40°C . Finally, obvious antiferroelectric characteristics are observed around 80°C . That means, the ferroelectric-antiferroelectric transition occurs between 20°C - 40°C .

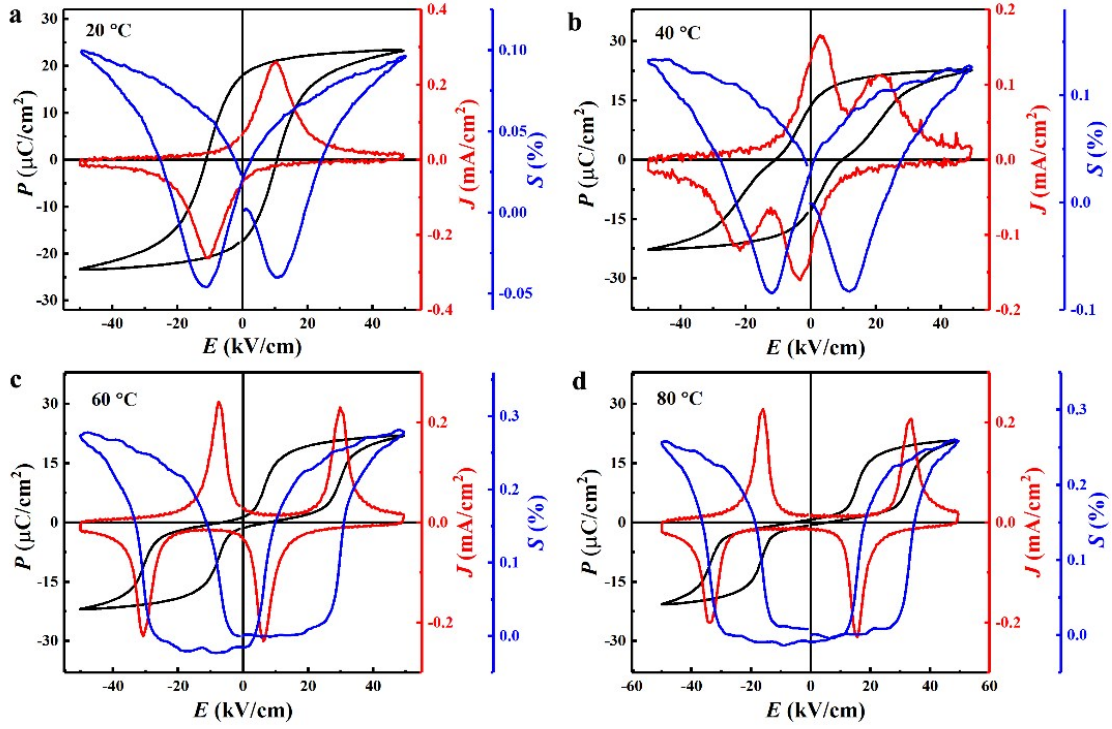


Figure S9. Temperature-dependent P - E , J - E and S - E curves of 0.7PNZST-0.3ZnO composite ceramics. Similar with PNZST-0.1ZnO and PNZST-0.2ZnO composites, this composite shows ferroelectric characteristics at $T \leq 20$ °C, and antiferroelectric characteristics tend to appear around 40 °C. Finally, obvious antiferroelectric characteristics are observed around 60 °C. That means, the ferroelectric-antiferroelectric transition occurs around 40 °C.

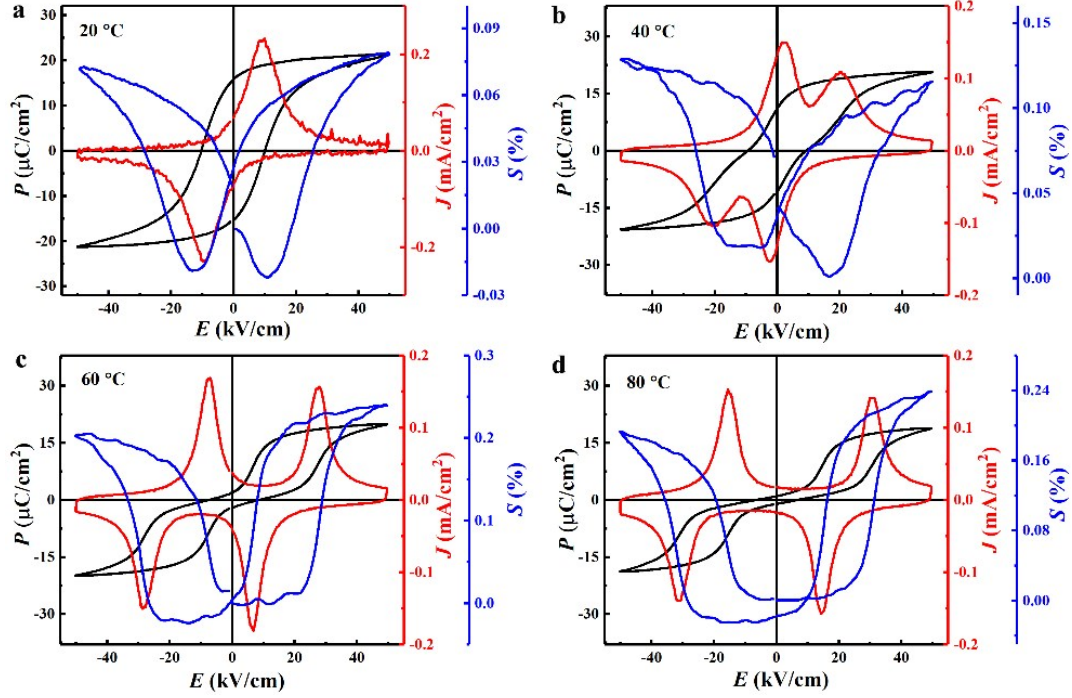


Figure S10. Temperature-dependent P - E , J - E and S - E curves of 0.6PNZST-0.4ZnO composite ceramic. Similar with PNZST- x ZnO with $x = 0.1, 0.2$ and 0.3 , this composite shows ferroelectric characteristics at $T \leq 20^\circ\text{C}$, and antiferroelectric characteristics tend to appear around 40°C , obvious antiferroelectric characteristics are observed 60°C . Therefore, the ferroelectric-antiferroelectric transition occurs around 40°C .

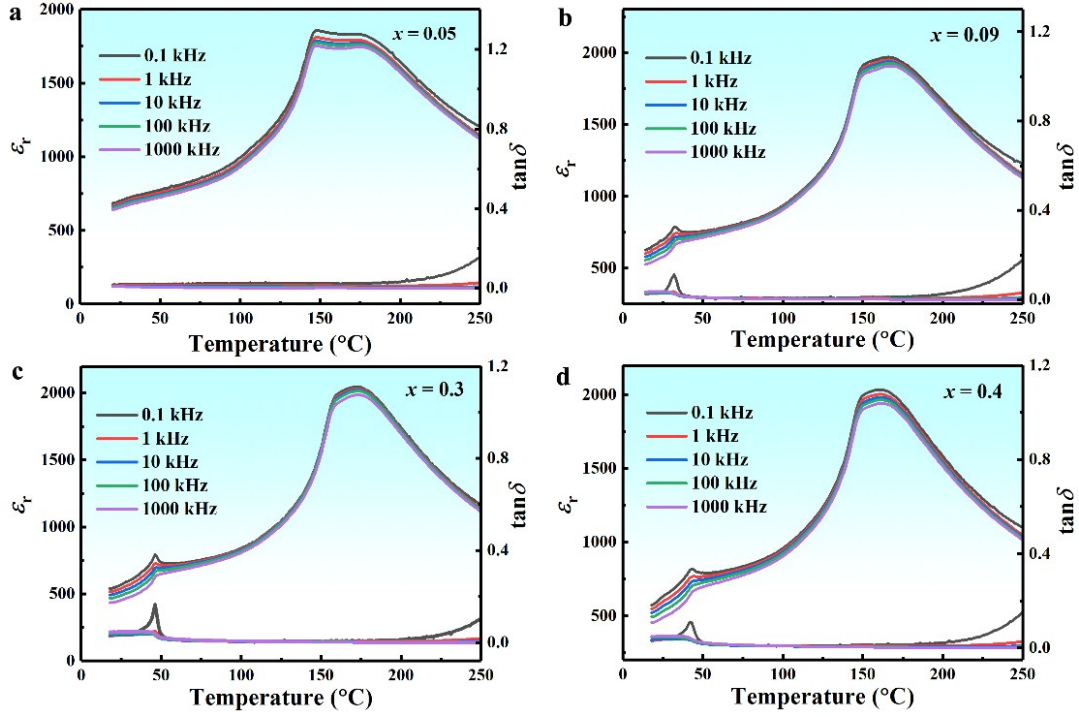


Figure S11. Temperature-dependent dielectric properties. (a) No ϵ_r and $\tan\delta$ peaks around room temperature can be detected in $x = 0.05$ sample, which indicates that ZnO content is not enough to form room temperature ferroelectric state in antiferroelectric PNZST. On the contrary, obvious ϵ_r and $\tan\delta$ peaks can be seen at 32 °C, 46.2 °C and 43 °C, respectively, in (b) $x = 0.09$, (c) $x = 0.3$ and (d) $x = 0.4$ samples, indicating the formed room temperature ferroelectric state. Combined with the analysis of Figure 3, it can be concluded that these peaks arise from ferroelectric-antiferroelectric transition.

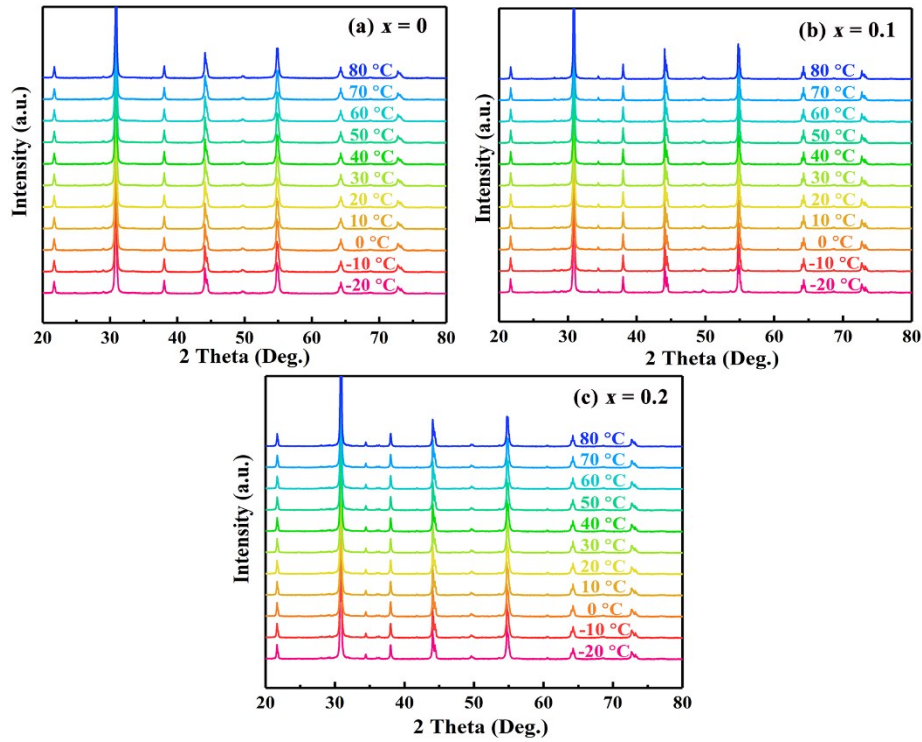


Figure S12. Temperature-dependent XRD patterns of $(1-x)\text{PNZST}-x\text{ZnO}$ ($x = 0, 0.1$ and 0.2) ceramics. In the measuring temperature range, PNZST shows pseudotetragonal crystal structure based on structure refinement, consistent with other reports.^{7,9} The temperature dependent cell volume is given in Fig. 4b. Please note that the pseudotetragonal structure is preserved across the FE-AFE transition due to the similar XRD patterns. However, it is generally accepted that PNZST has ferroelectric rhombohedral structure and antiferroelectric pseudotetragonal structure.^{10,11} We believe two possible reasons should be considered. One is that this composition lies around the boundary between rhombohedral and pseudotetragonal structure,¹² and the other is that this composition shows significant thermal hysteresis.⁹ Our further electric-field dependent SXRD will reveal their different structure in ferroelectric states. For $x = 0.1$ and 0.2 composite ceramics, in the whole measuring temperature range, the PNZST in this composite also shows pseudotetragonal crystal structure and the lattice parameters are given in Fig. 7 and 8.

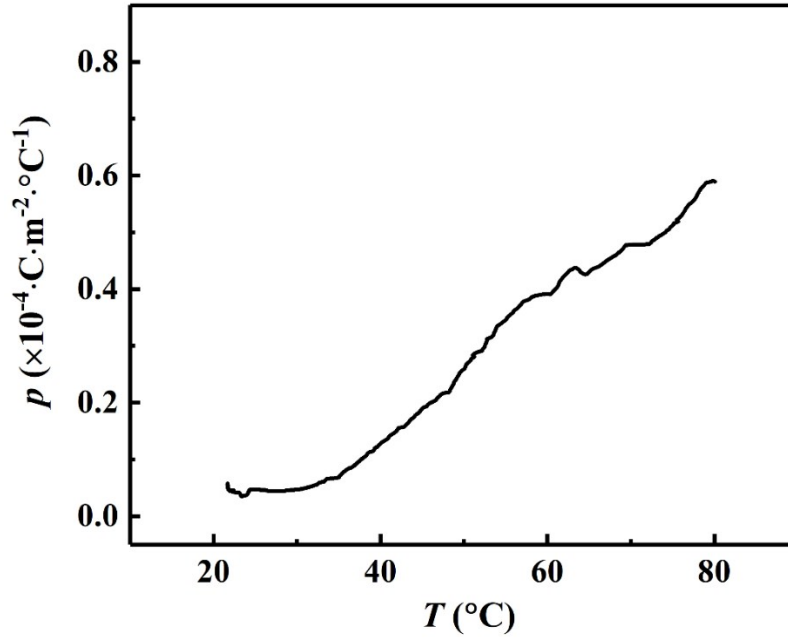


Figure S13. Temperature dependent p value of the ZnO ceramics. In the whole measuring temperature range from 20 °C to 80 °C, the pyroelectric coefficient p value is $0.05\sim 0.63 \times 10^{-4} \cdot \text{C} \cdot \text{m}^{-2} \cdot \text{C}^{-1}$, about 3-order of magnitude lower than the peak p value in the 0.9PNZST-0.1ZnO composite. Please note that the p value of our ZnO ceramics is close to other reports on ZnO.^{13,14} More importantly, one cannot observe any pyroelectric peak around 39°C. Thus, we believe that ZnO in the (1- x)PNZST- x ZnO composite ceramics has negligible contribution to the measured high pyroelectric performance.

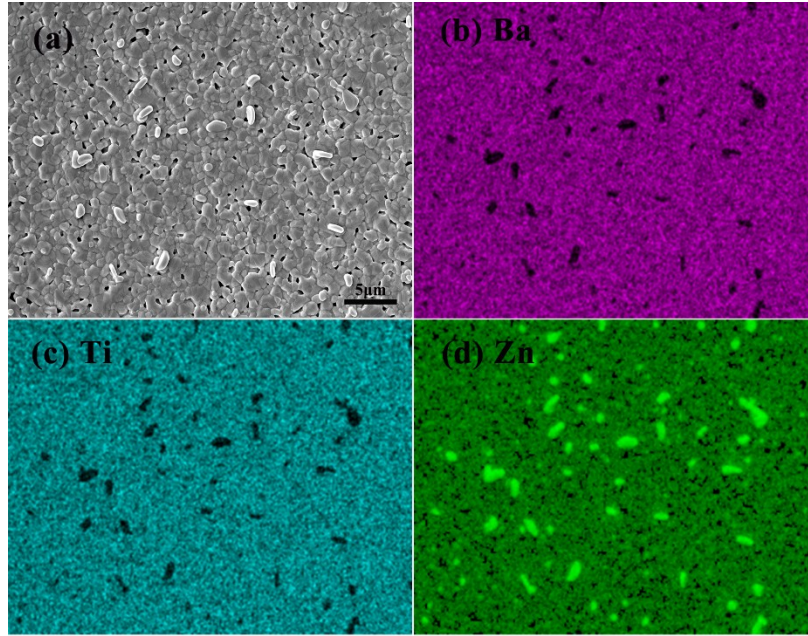


Figure S14. Typical SEM micrograph (a) and element distribution (b-d) of the $0.9\text{BaTiO}_3\text{-}0.1\text{ZnO}$ composite ceramics. Obviously, Ba and Ti occupy most 3D connected areas while Zn occupies 0D isolated areas. By comparing with Supplementary Fig. 3, we can see that the $\text{BaTiO}_3\text{-}x\text{ZnO}$ composites have similar 0-3 type composite microstructure as $(1-x)\text{PNZST-}x\text{ZnO}$ composites, thus this supporting material system is helpful to clarify the possible microstructure contribution to pyroelectric performance of $(1-x)\text{PNZST-}x\text{ZnO}$. Moreover, please note that BaTiO_3 is a well-known ferroelectric material with Curie temperature $T_c \sim 120^\circ\text{C}$, so this $(1-x)\text{BaTiO}_3\text{-}x\text{ZnO}$ system is also helpful to reaffirm the unique role of antiferroelectric PNZST in the $(1-x)\text{PNZST-}x\text{ZnO}$ composites. Scale bar: $5\ \mu\text{m}$.

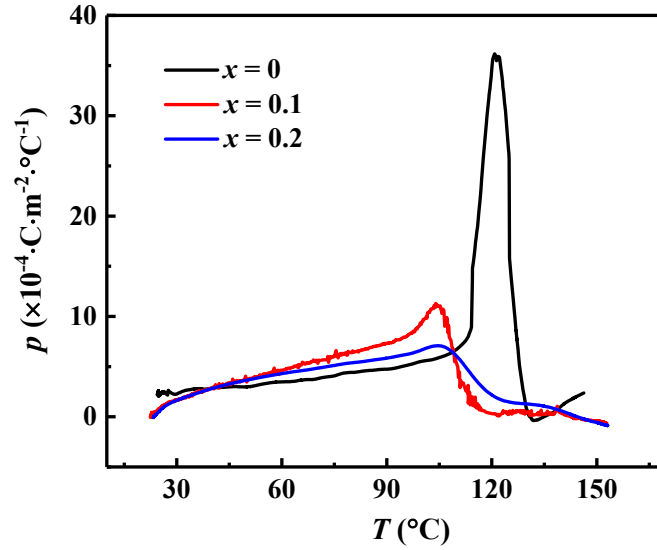


Figure S15. Temperature dependent pyroelectric coefficient p of the $(1-x)\text{BaTiO}_3-x\text{ZnO}$ composite ceramics. Three important features should be addressed. (1) The p of BaTiO_3 around T_c is $\sim 36 \times 10^{-4} \cdot \text{C} \cdot \text{m}^{-2} \cdot \text{C}^{-1}$, close to other report.¹⁵ When ZnO is introduced, the p value around T_c tends to decrease with increasing ZnO content (x value), which is reasonably attributed to decreased ferroelectric BaTiO_3 content. At other temperatures, the p value of $(1-x)\text{BaTiO}_3-x\text{ZnO}$ composite ceramics is extremely low and almost composition-independent. Hence, we can believe that BaTiO_3 has dominant contribution to pyroelectric effect in this $(1-x)\text{BaTiO}_3-x\text{ZnO}$ composites, in other words, ZnO has negligible contribution. This is consistent with the above supporting experiment on pure ZnO ceramics (Figure S12). In addition, the nearly composition-independent pyroelectric property of $(1-x)\text{BaTiO}_3-x\text{ZnO}$ clearly confirms that the possible artifacts like trapped charges/ions in composites cannot induce high pyroelectric performance. Since $(1-x)\text{PNZST}-x\text{ZnO}$ has similar 0-3 type microstructure with $(1-x)\text{BaTiO}_3-x\text{ZnO}$, it is reasonable to believe that in $(1-x)\text{PNZST}-x\text{ZnO}$ case, the contribution from possible artifacts is also negligible. (2) For each $(1-x)\text{BaTiO}_3-x\text{ZnO}$ composite ceramic, the p value reaches the maximum of $\sim 36 \times 10^{-4} \cdot \text{C} \cdot \text{m}^{-2} \cdot \text{C}^{-1}$, about 2-order of magnitude lower than that of peak p value in $0.9\text{PNZST}-0.1\text{ZnO}$. (3) For each $(1-x)\text{BaTiO}_3-x\text{ZnO}$ composite ceramic, the peak p value is observed around $T_c \sim 120^\circ\text{C}$, but not around 39°C which is the peak temperature of p value in $0.9\text{PNZST}-0.1\text{ZnO}$. By comparing Figure S14 with Fig. 3, it is safe to conclude that the observed high pyroelectric performance near room temperature in $\text{PNZST}-\text{ZnO}$ composite ceramics comes from FE-AFE transition of PNZST .

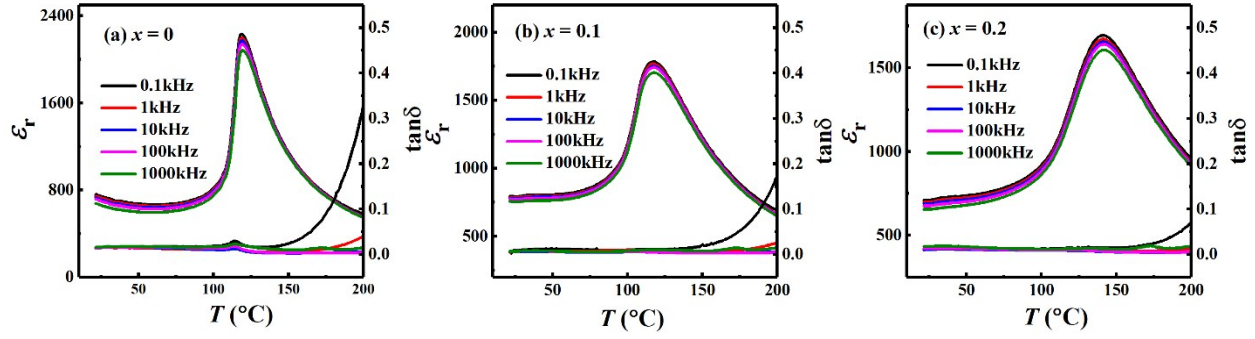


Figure S16. Temperature dependent dielectric property of the poled $(1-x)\text{BaTiO}_3-x\text{ZnO}$ composite ceramics. As can be seen, there is no dielectric peak around room temperature, which is different from that of PNZST-ZnO composites. Actually, this dielectric property is consistent with pyroelectric property shown in Figure S14.

Table S1. Comparison of pyroelectric coefficients of PNZST-ZnO ceramics with that of other pyroelectric materials around room temperature and human body temperature (25 °C - 40 °C).

| sample | T (°C) | P $10^{-4} \text{ C} \cdot \text{m}^{-2} \cdot \text{K}^{-1}$ | ϵ_r | $\tan\delta$ | F_v ($10^{-2} \text{ m}^2 \cdot \text{C}^{-1}$) | F_d ($10^{-5} \text{ Pa}^{-1/2}$) | F_i ($10^{-10} \text{ m} \cdot \text{V}^{-1}$) |
|--|-------------|--|--------------|--------------|--|--|---|
| PNZST-0.1ZnO (this work) | 39 | 1053.9 | 753.1 | 0.0135 | 1249.4 | 876.3 | 832.7 |
| PMnN-PMS-PZ _{0.95} T _{0.05} | 25 | 26.5 | 265 | 0.009 | | | |
| Mn-PBLZST(70/25/5) | 27.5 | 140 | 4700 | 0.012 | | 25 | |
| PLZST(75/16/9) | 32 | 36 | | | | | 13.2 |
| PLZST(57/38/7) | 25 | 35 | | | | | |
| Mn-PNZT(95/5) | 32 | 9.15 | 270 | 0.002 | 15.3 | 16.74 | 3.7 |
| La-PZST | 38 | 100 | | | | | |
| PMNT:Mn | 38 | 12 | | | | | |
| PIMNT:Mn | 38 | 8 | | | | | |
| PIMNT | 38 | 7 | | | | | |
| 0.89BNT-0.06BT-0.05KNN | 27 | 6 | 2250 | 0.055 | | | |
| CSBN | 25 | 1.24 | 328 | 0.033 | 2.03 | 0.61 | 0.6 |
| SBN | 25 | 2.05 | 971 | 0.039 | 1.14 | 0.53 | 0.98 |
| N ₄₄ B ₄₇ T ₉₄ -6BT | 34 | 140 | | | | | |
| BCT-BST | 25 | 2.05 | 3500 | 0.025 | 0.32 | 0.41 | 1 |
| BNT-BZT | 25 | 5.7 | 1052 | 0.04 | 2.18 | 1.05 | 2.03 |
| KNN-BKT | 25 | 2.18 | 980 | 0.035 | 1.14 | 0.57 | 0.994 |
| BNT-BT-ST | 25 | 5.7 | 1278 | 0.109 | 1.8 | 0.589 | 2.08 |
| BNT-BA-KNN | 25 | 3.7 | 514 | 0.029 | 2.89 | 1.15 | 1.32 |
| La -BNT-6BT | 25 | 7.42 | 650 | 0.065 | 0.048 | 1.4 | 2.65 |
| La-NKBT film | 38 | 4 | | | | 2 | |
| TGS crystal | 35 | 5.5 | 55 | 0.025 | 43 | 6.1 | 2.12 |
| DTGS | 40 | 5.5 | 43 | 0.02 | 60 | 8.3 | |
| ATGSAS | 25 | 7.0 | 32 | 0.01 | 99 | 16.6 | |
| LiTaO ₃ crystal | 25 | 2.3 | 47 | 0.0005 | 17 | 15.7 | 0.72 |
| KNLNTS | 25 | 1.9 | 1520 | 0.0181 | 0.7 | 0.598 | 0.931 |
| NKLBT-0.05BT | 25 | 3.6 | | | 0.017 | | 1.27 |
| PMnN-PMS-PZT(Zr95) | 28 | 26.5 | | | | | |
| PMnN-PMS-PZT(Zr96) | 34 | 16 | | | | | |
| BST0 | 26 | 10 | | | | 2.5 | |
| BST _(PMMA) | 25 | 80 | | | | 24 | |
| BST _(CNT1) | 25 | 95 | | | | 32 | |

References

1. H. Liu, J. Chen, L. L. Fan, Y. Ren, Z. Pan, K. V. Lalitha, J. Rödel and X. R. Xing, *Phys. Rev. Lett.* 2017, **119**, 017601.
2. F. Xue, L. Liang, Y. Gu, I. Takeuchi, S. V. Kalinin and L. Q. Chen, *Appl. Phys. Lett.* 2015, **106**, 012903.
3. J. Zhang, Z. Pan, F.-F. Guo, W.-C. Liu, H. Ning, Y.B. Chen, M.-H. Lu, B. Yang, J. Chen, S.-T. Zhang, X. Xing, J. Rödel, W. Cao and Y.-F. Chen. *Nat. Commun.* 2015, **6**, 6615.
4. Y. P. Guo, Y. Liu, R. L. Withers, F. Brink and H. Chen, *Chem. Mater.*, 2011, **23**, 219.
5. H. S. Wang, Y. C. Liu, T. Q. Yang and S. J. Zhang, *Adv. Funct. Mater.*, 2019, **29**, 1807321.
6. W. Y. Pan, C. Q. Dam, Q. M. Zhang and L. E. Cross, *J. Appl. Phys.*, 1989, **66**, 6014.
7. M. Daniels, D. Damjanovic, A. Studer, M. Hoffman and J. Jones, *J. Appl. Phys.*, 2007, **101**, 104108.
8. T. Rojac, M. Kosec and D. Damjanovic, *J. Am. Ceram. Soc.*, 2011, **94**, 4108.
9. J. Frederick, X. L. Tan and W. Jo, *J. Am. Ceram. Soc.*, 2011, **94**, 1149.
10. M. Avdeev, J. D. Jorgensen, S. Short, G. A. Samara, E. L. Venturini, P. Yang and B. Morosin. *Phys. Rev. B*, **2006**, 73, 064105.
11. X. L. Tan, J. Frederick, C. Ma, W. Jo and J. Rödel, *Phys. Rev. Lett.*, 2010, **105**, 255702.
12. H. He and X. L. Tan, *J. Phys.: Condens. Matter.*, 2007, **19**, 136003.
13. Y. Yang, W. Guo, K. C. Pradel, G. Zhu, Y. Zhou, Y. Zhang, Y. Hu, L. Lin and Z. L. Wang, *Nano Lett.*, 2012, **12**, 2833.
14. J. Albertsson, S.C. Abrahams and Å. Kvik, *Acta Cryst. B*, 1989, **45**, 34.
15. K.K. Deb, M.D. Hill and J.F. Kelly, *J. Mater. Res.* 1992, **7**, 3296.